ACS OMEGA

Open Access



http://pubs.acs.org/journal/acsodf

Article

# Zircon-Type $CaCrO_4$ Chromite Nanoparticles: Synthesis, Characterization, and Photocatalytic Application for Sunlight-Induced Degradation of Rhodamine B

Naeem Akbar, Muhammad Javed,* Ayaz Arif Khan,* Asad Masood, Naeem Ahmed, Raja Yasir Mehmood, Said Nasir Khisro, Muhammed Ali Shaikh Abdul, Muhammad Aniq Shazni Mohammad Haniff,* and Attaullah Shah

Cite This: *ACS Omega* 2023, 8, 30095−30108

Read Online

ACCESS | Metrics & More | Article Recommendations

**ABSTRACT:** The degradation of organic dye pollutants is a critical environmental issue that has garnered significant attention in recent years. To address this problem, we investigated the potential of $CaCrO_4$ chromite (CCO) as a photocatalyst for the degradation of cationic and anionic dye solutions under sunlight irradiation. $CaCrO_4$ was synthesized via a sol−gel auto-combustion route and sintered at 900 °C. The Rietveld refined XRD profile confirmed the zircon-type structure of $CaCrO_4$ crystallized in the tetragonal unit cell with *I*41/*amd* space group symmetry. The surface morphology of the sample was investigated by field emission scanning electron microscopy (FESEM), which revealed the polyhedral texture of the grains. Energy-dispersive X-ray spectroscopy (EDX) and X-ray photoelectron spectroscopy (XPS) studies were carried out to analyze the elemental composition and chemical states of the ions present in the compound. Fourier transform infrared (FT-IR) spectroscopy analysis revealed the vibrational modes corresponding to the tetrahedral and dodecahedral metal oxide bonds. The optical band gap was approximated to be in the range of 1.928 eV by using the Tauc relation. The $CaCrO_4$ catalyst with different contents (5, 20, 35, and 50 mg) was investigated for its photocatalytic performance for the degradation of RhB dye solution under sunlight irradiation using a UV−Vis spectrometer over the experimental wavelength range of 450−600 nm. The degradation efficacy increased from 70.630 to 93.550% for 5−35 mg and then decreased to 68.720% for 50 mg in 140 min under visible light illumination. The comparative study demonstrates that a higher degradation rate was achieved for cationic than anionic dyes in the order RhB > MB > MO. The highest deterioration (93.80%) was achieved for the RhB dye in 140 min. Equilibrium and kinetic studies showed that the adsorption process followed the Langmuir isotherm and pseudo-second-order models, respectively. The maximum adsorption capacity of 21.125 mg/g was observed for the catalyst concentration of 35 mg. From the cyclic test, it has been observed that the synthesized photocatalyst is structurally and morphologically stable and reusable. The radical trapping experiment demonstrated that superoxide and hydroxyl radicals were the primary species engaged in the photodegradation process. A possible mechanism for the degradation of RhB has been proposed. Hence, we conclude that $CaCrO_4$ can be used as an efficient photocatalyst for the remediation of organic dye pollutants from the environment.

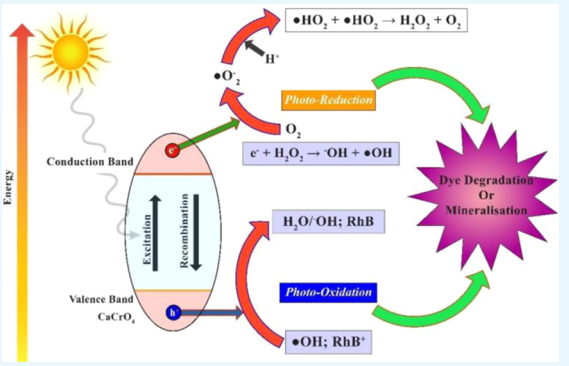


## 1. INTRODUCTION

Environmental problems have become more prominent globally due to rapid population growth, industrialization, and ongoing technological developments that have significantly increased the number of organic pollutants exhibiting carcinogenic effects on natural resources, aquatic life, and human beings.[1−4] Synthetic dyes are a significant environmental concern due to their high solubility, high chemical stability, and their toxic nature and most of the dyes contain aromatic rings, which cause carcinogenic and mutagenic effects.[5] Specifically, the amount of organic synthetic dyes discharged into the environment is increasing yearly from various industries such as leather goods, colored paper, cosmetics, and consumer food manufacturing.[6] Dumping these dyes into water not only changes their color but also

Received: April 11, 2023
Accepted: June 26, 2023
Published: August 7, 2023

disrupts the oxygen level. Therefore, the removal of organic pollutants from natural resources is a significant task, and developing an effective approach is critical.[7]

In the last few decades, many efforts have been devoted to removing organic dye pollutants from environmental resources. One of the most significant environmental concerns is wastewater purification, which remains a significant challenge in reducing health risks.[8,9] From a public health and environmental perspective, it is essential to remove the organic dye pollutants by employing various technologies. Many physical and chemical methods for wastewater treatment have been reported, including electrochemical, oxidation, reduction, flocculation, adsorption, and precipitation, among others. However, these techniques exhibit various inadequacies in degrading organic contaminants.[9,10]

The semiconductor-based metal oxide is thought to be active under UV and visible light to tackle the issues of fossil energy and environmental pollution. Recently, the photodegradation of organic pollutants using semiconductor metal oxide has been identified as a promising water purification protocol because of its significant ability to degrade a wide range of toxic and nontoxic organic pollutants and antibiotics in wastewater without involving complex technologies.[11] Metal oxide ceramic materials with an $ABO_4$ structure, including scheelite, zircon, and powellite, have been investigated due to their intriguing manifold physical characteristics.[12] In comparison to their bulk counterparts, low-dimensional ceramic metal oxides have a high surface-to-volume ratio, surface defects, and quantum effects that exhibit intriguing optical, catalytic, and dielectric characteristics. Based on the literature, metal oxide-based semiconductor photocatalysts tune their structural, morphological, and optical properties, which are critical for the degradation of organic pollutants.[13] The $ABO_4$ structures are mainly semiconductors and play a significant role in the photocatalytic process which might be attributed due to the low band gap energy. Previous reports have drawn serious attention to the possibility of the application of $ABO_4$ compounds in the photocatalytic degradation of organic dyes and salicylic acid.[14,15] Among the $ABO_4$ compounds, the calcium chromite $CaCrO_4$ zircon-type structure has gained significant attention due to their technological application in various fields, which can help to understand the details of physical phenomena at the nanoscale both for academic and industrial purposes.[16] $CaCrO_4$ is a member of the chromite family with space group *I*41/*amd* and a zircon-like symmetry that has been thoroughly investigated due to its several interesting properties.[17] To date, several studies have investigated the photodegradation of organic dye pollutants by using several zircon-based metal oxides as photocatalysts.[18] However, the use of $CaCrO_4$ nanoparticles as adsorbents for organic dye removal has not been explored. Therefore, $CaCrO_4$ with space group *I*41/*amd* has been proposed as a potential candidate for removing various organic dye pollutants, antibiotic remediation, and wastewater treatment.

The photocatalytic degradation process in zircon-like systems is closely related to the synthesis route, which has a substantial influence on the structural and morphological properties that are vulnerable to photodegradation.[19] Different wet chemical routes have been reported for the preparation of $CaCrO_4$ chromites, such as formalin-sol−gel,[20] hydrothermal,[21] the standard solid-state reaction method,[22] and the chemical coprecipitation method.[23] The synthesis technique, calcination temperature, and substantial element all have an impact on the physicochemical characteristics of the catalyst.[24] The sol−gel auto-combustion approach has been demonstrated as the most effective method for synthesizing the $ABO_4$ metal oxide due to its high purity, improved crystallinity, superior chemical homogeneity, and ecologically admissible handling of chemicals and equipment.[22,23] An exothermic reaction premised on self-sustaining xerogel and a thermally induced anionic redox reaction are employed in this approach. An aqueous solution comprising appropriate metal salts as oxidizing agents and organic complexes as reductants is used as a precursor. This renders the sol−gel auto-combustion process suitable for tailoring the distribution of metal cations at the tetrahedral and dodecahedral sites of the metal oxide zircon system by selecting an appropriate chelating agent, which burns the unwanted phase out of the compound.[25,26] In this study, we employed the sol−gel auto-combustion technique to synthesize $CaCrO_4$ as a photocatalyst and analyze its structure and morphology. The resulting structure and morphology of the photocatalyst were thoroughly investigated. The photocatalyst has been assessed for the degradation of synthetic pigments such as rhodamine B (RhB), methylene blue (MB), and methyl orange (MO) under UV light irradiation in order to evaluate its photocatalytic efficiency. In addition, several influential variables, such as contact time and dosage of the adsorbent, comparison of organic pollutants, recyclability, radical trapping test, and dye degradation mechanism were proposed to determine their impact on the photocatalytic process. The isotherms of adsorption and kinetic models were also explored to find the most favorable ones to demonstrate the process of adsorption.

## 2. EXPERIMENTAL SECTION

**2.1. Synthesis.** The tetragonal $CaCrO_4$ chromite was synthesized by the wet chemical sol−gel auto-combustion route. The precursors used with high purity were calcium nitrate [$Ca(NO_3)2.6H_2O$], chromium nitrate [$Cr(NO_3)$-$3.9H_2O$], and citric acid [$C_6H_8O_6$]. Nitric acid was used as the fuel in the combustion process, and metal nitrates were used as the oxidizing agent. The stoichiometric amounts of metal nitrates were dissolved in deionized (DI) water while stirring. The citrate solution was then added dropwise to the nitrate solution under continuous stirring, with the nitrate-to-citrate ratio set at 1. The solution was neutralized by adding ammonium hydroxide (NH4OH). The resulting highly viscous gel was evaporated by heating it on a hot plate at 120 °C under vigorous stirring for about 3 hours. The gel was then heated to around 300 °C, which released a substantial volume of gases from the gel. After a short interval of heating, the ignition temperature was reached, and a self-combustion process started. This resulted in a gray, fluffy, and malleable powder, which was collected, ground, and calcined in an electric furnace at 900 °C for 10 h.

**2.2. Photocatalytic Test.** The photocatalytic efficacy of the $CaCrO_4$ catalyst was investigated by the degradation of rhodamine B (RhB) under sunlight irradiation. A 5 ppm stock solution of RhB was prepared in DI water and 5 mg of the catalyst was added to 10 mL of RhB solution. The resulting solution was kept in the dark at room temperature and stirred for 1 h to obtain maximum homogeneity in the mixture, ensuring the maximum absorption of organic pollutants on the photocatalytic surface and availability of oxygen for the photodegradation reaction. Subsequently, the reaction mixture (dye/catalyst) was exposed to sunlight in beakers. At regular


https://doi.org/10.1021/acsomega.3c02457
ACS Omega 2023, 8, 30095−30108

intervals of 20 minutes, samples were taken, and the absorbance for each time interval was recorded using a UV−Vis spectrometer over the experimental wavelength range of 450−600 nm at room temperature.

**2.3. Characterization.** X-ray diffraction (XRD) using a DMAX-3A, instrument with Cu K$\alpha$ radiation at a wavelength of 1.54 Å was employed to investigate the structural and phase analysis of the $CaCrO_4$ chromite. The XRD spectrum was scanned in a 2$\theta$ range of 10−80° with a step size of 0.05°. The morphology of the sample was examined using field emission scanning electron microscopy (FESEM, Zeiss Merlin), and the elemental composition was determined by the energy-dispersive X-ray (EDX) study. X-ray photoelectron spectroscopy (XPS) was conducted using a ULVAC-PHI Quantera II instrument with Al K source having an energy of 1486.6 eV to explore the chemical states of the elements in the sample. The high-resolution spectra were fitted using the CasaXPS software (Ver. 2.3.22PR1.0). The Shirley-type background with a Gaussian−Lorentzian spectral line shape (30% Lorentzian component) was used in the curve-fitting method. The binding energy of the "neutral" C peak, including the C−C and C−H components, was used to calibrate XPS spectra at 285.0 eV. FT-IR spectroscopy (Perkin Elmer Spectrum 100 series) was utilized to examine the chemical bonds and functional groups in the sample. The photocatalytic performance of the $CaCrO_4$ catalyst against rhodamine B dye was evaluated using a UV−Vis spectrometer (Data Stream 3000 series) with different time intervals ranging from 20 to 140 min with a time difference of 20 min.

## 3. RESULTS AND DISCUSSION

**3.1. Structural and Microstructural Analysis.** Figure 1 shows the X-ray powder diffraction profile of the $CaCrO_4$ chromite synthesized by the sol−gel self-combustion method and calcined at 900 °C. The diffraction peaks are sharp and well-defined, matching the JCPDS standard for $CaCrO_4$ with card number 87−1647.[17] The diffraction peaks are indexed to the tetragonal zircon-type structure with *I*41/*amd* space group, confirming the single-phase formation of $CaCrO_4$. The Rietveld refinement analysis was performed using the Fullprof program, which provided detailed information about the structural parameters such as lattice parameters, space group symmetry, unit cell volume, and atomic fractional coordinates. The experimental XRD profile is shown by red symbols (Figure 1), the calculated results by continuous black lines, the standard positions of Bragg reflections by blue vertical bar ticks, and the difference between observed and calculated XRD patterns by a pink solid line. The refinement results are tabulated in Table 1, and the reliability of the fit with the experimental pattern was confirmed by the discrepancy R-factor.

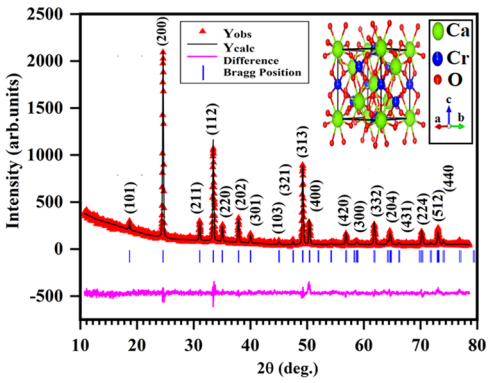


**Figure 1.** Rietveld refined X-ray diffraction profile of $CaCrO_4$ (the inset illustrates the unit cell crystal structure).

Furthermore, the average crystallite size of the $CaCrO_4$ tetragonal system was calculated by using the Debye−Scherrer's (D−S) equation[27]

$$D = \frac{K\lambda}{\beta \cos\theta} \tag{1}$$

eq 1 relates the crystallite size ($D$) to the full width at half maximum (FWHM) of the XRD peak, and other factors such as the particle shape factor ($K$), the wavelength of the X-ray source ($\lambda$), and diffraction angle ($\theta$). The average crystallite size was calculated using the linear fit of eq 1 to the cos$\theta$ versus $1/\beta$ plot as shown in Figure 2a, resulting in a size of and it was found to be 75.3102 nm. However, the Debye−Scherrer (D−S) equation was used to calculate crystallite size but does not account for lattice distortion and micro-strain induced in the structure.[27] To analyze the effect of distortion on crystallite size, the Williamson−Hall (W−H) analysis was performed. The W−H analysis is based on the integral breadth approach, which separates the peak broadening caused by the crystallite size and micro-strain in the structure from the diffraction peak.[28] The W−H equation is expressed as[28]

$$\beta \cos\theta = \frac{k\lambda}{D} + 4\varepsilon \sin\theta \tag{2}$$

In eq 2, the strain induced in the structure is symbolized by $\varepsilon$. Figure 2b depicts the fit of eq 2 to the $\beta \cos\theta$ versus 4 sin$\theta$ plot. The lattice strain and average crystallite size were calculated by determining the slope and intercept of the graph which are $2.2730 \times 10^{-4}$ and 90.1420 nm, respectively. The W−H analysis yielded a slightly greater crystallite size than that estimated by the D−S equation. This difference can be attributed to the inclusion of lattice distortion in the W−H equation, which affects the peak broadening and hence the estimation of crystallite size. The crystal information deduced by Rietveld refinement was further processed by the VESTA program to comprehend the unit cell of the $CaCrO_4$ zircon structure.[29] The unit cell structure of the $CaCrO_4$ chromite system is displayed in the inset of Figure 1. The tetrahedral sites contain $Cr^{\wedge}(3+)$ cations, while $Ca^{\wedge}(+2)$ cations are located at the dodecahedral sites. The bond lengths and bond angles of $CaCrO_4$ chromite were determined further using BondStr software, which is built into the Fullprof package and is shown in Table 1. The refined results were also employed to study the distribution of electron density (DE) using the Fourier transform of the structural factor.[30] The electron density distribution helps to visualize the type of chemical binding and structural distribution in the unit cell of the $CaCrO_4$ network. Two- and three-dimensional (2D and 3D) Fourier maps of the ED distribution in $CaCrO_4$ along xz-directions with a Fourier limit of 1 Å are shown in Figure 2c,d. The 2D map with yellow contours indicates the ED of the Ca atom, while those centered with magenta colors represent the d-electrons in the bound Cr atom. The contours are centered with light green color, indicating the ED of 2p electrons in the O atom. The 3D Fourier map of the $CaCrO_4$ unit cell exhibits a chicken-wire style of ED distribution, with peaks of


https://doi.org/10.1021/acsomega.3c02457
ACS Omega 2023, 8, 30095−30108

**Table 1. Structural Results Approximated from the Rietveld XRD Profile Analysis of the $CaCrO_4$ Chromite**

| chromite system | | | $CaCrO_4$ | | | |
|---|---|---|---|---|---|---|
| structural parameters | space group | *I*41/*amd* | atom | Wyckoff positions | | |
| | lattice parameters | | | *x*/*a* | *y*/*b* | *Z*/*c* |
| | $\alpha = \beta = \gamma$ | 90 | Ca | 0.0000 | 0.0000 | 0.0000 |
| | *a* (Å) | 7.2445 | Cr | 0.0000 | 0.0000 | 0.5000 |
| | *b* (Å) | 7.2445 | O | 0.0000 | 0.1886 | 0.3400 |
| | *c* (Å) | 6.2895 | bondstr results | | | |
| | unit cell volume (Å$^3$) | 330.0904 | bond | bond distance | bond | bond angle |
| | $D_{D-S}$ | | $D_{W-H}$ | | micro-strain | |
| | 75.3102 | | 90.1420 | | $2.2730 \times 10^{-5}$ | |
| reliable factors | $R_F$ (%) | 8.9703 | Ca−O | 2.5379 | Ca−O−Ca | 22.8530 |
| | $R_p$ (%) | 84.6000 | Ca−Ca | 3.9488 | O−Ca−Ca | 43.9200 |
| | $R_{exp}$ (%) | 27.8800 | Ca−Cr | 3.1447 | O−Ca−O | 87.6850 |
| | $R_{wp}$ (%) | 32.4000 | Cr−O | 1.6974 | O−Cr−O | 107.5360 |
| | $\chi^2$ (%) | 1.35 | Cr−Cr | 2.9483 | Cr−O−Cr | 52.9640 |

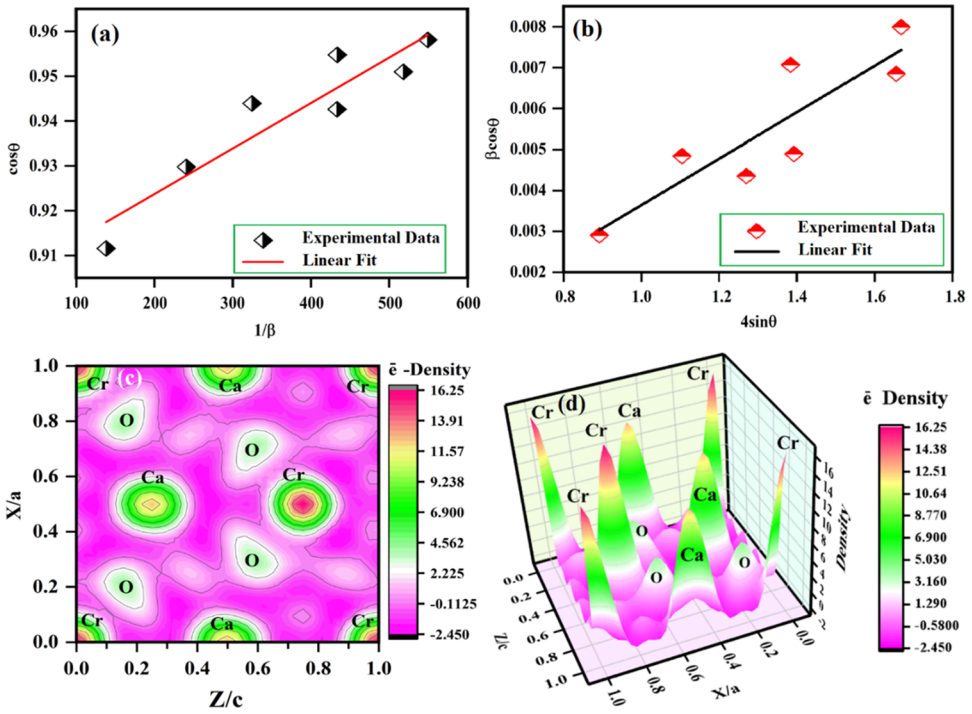


**Figure 2.** (a, b) D−S, (b) W−H plots and (c) 2D and (d) 3D electron density distributions of $CaCrO_4$ tetragonal chromite.

maximum intensity indicating Cr atom contribution and peaks with lower ED clouds reflecting the Ca atom. In this case, the ED of the O atom is comparatively small and more subdued. From these observations, it has been observed that there is no considerable electron sharing between the metal cations, suggesting that the nature of bonding in $CaCrO_4$ is ionic.

Figure 3a shows transmission electron microscopic (TEM) image of the synthesized photocatalyst with the magnification of 100 nm. The figure reveals that the compound exhibits a cluster-like geometry. Further, the high-resolution transmission electron microscopic (HRTEM) graph of CaCrO4 is shown in Figure 3b. The top inset of Figure 3b illustrates the inter-planer spacing, which was found to be in the range of 0.186 nm based on the TEM micrograph. Figure 3b bottom inset displays the selected area electron diffraction (SAED) spectra of CCO chromite. The polycrystalline character of the $CaCrO_4$ is suggested by the nearly circular concentric rings with bright spots, and the prominent peaks in the SAED diffractogram may

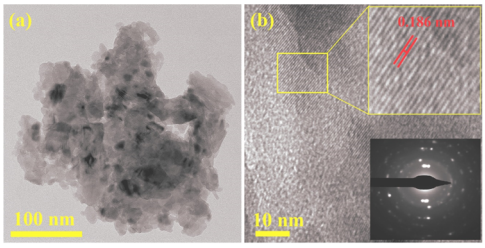


**Figure 3.** (a, b) Transmission electron microscopic images. Top and bottom insets are HRTEM and SAED images of the CCO chromite.

correspond to the reflection planes of CCO chromite (101), (200), (112), (220), (202), (301), and (313), respectively. These results agree with those deduced from the XRD analysis of the sample.

The chemical bonds of the $CaCrO_4$ catalyst were examined using FT-IR spectroscopic analysis, and the corresponding


https://doi.org/10.1021/acsomega.3c02457
ACS Omega 2023, 8, 30095−30108

spectrum is illustrated in Figure 4. The vibration band at 3742 $cm^{-1}$ corresponds to the hydroxyl group absorbed on the

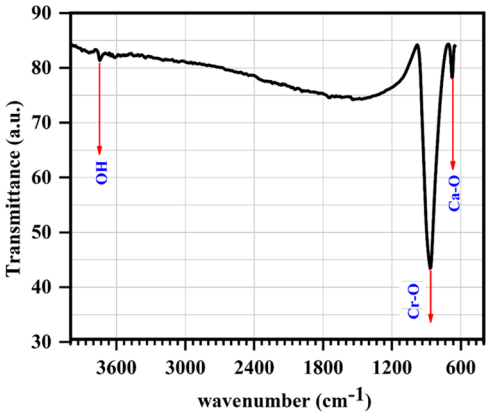


**Figure 4.** FT-IR spectra of the $CaCrO_4$ photocatalyst.

surface of the sample.[31] The vibrational modes appearing at 865, and 674 $cm^{-1}$ contributed to the stretching bands of Cr-O tetrahedral symmetry and Ca-O dodecahedral symmetry, respectively.[32,33] These results agree with the structural analysis.

The surface morphology of the $CaCrO_4$ powder sample calcined at 900 °C is shown in Figure 5a,b with two different

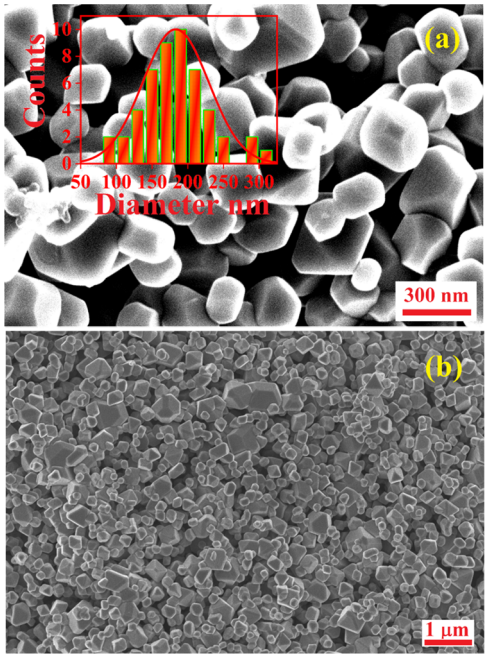


**Figure 5.** FESEM micrographs of the $CaCrO_4$ chromite with (a) high (inset shows particle size distribution) and (b) low magnification.

magnifications (50, 10 K). The variable crystal facets of the catalyst contribute to an active site for the adsorption and photodegradation processes.[34] From the FESEM images, it is obvious that the calcium chromite catalyst exhibits a polyhedral geometrical texture with considerable porosity and homogeneity of the structure. Furthermore, the average grain size was calculated using the ImageJ software to be about 170 ± 4.8 nm, as shown in the inset of Figure 5a.

The EDX spectrum of the $CaCrO_4$ catalyst at room temperature is shown in Figure 6a. The EDX results reveal the presence of Cr, O, and Ca elements in the compound. The inset of Figure 6a shows the elements' atomic and weight presents, which are in agreement with the compound initial stoichiometric ratio. The distribution of the elements is further illustrated by the elemental mappings shown in Figure 6b–d for Cr, O, and Ca, respectively. Thus, the EDX results indicate the absence of any impurity element in the compound.

Figure 7 depicts the XPS spectra of $CaCrO_4$ to analyze the surface chemistry, elemental composition, and chemical oxidation state present in the compound. Figure 7a depicts the C 1s peak of carbon comprising the C–C bond with a binding energy of 285 eV. When the sample is exposed to the atmosphere, the amount of carbon content is detected. The oxygen O 1s peaks in the $CaCrO_4$ sample are shown in Figure 7b, and the observable peaks in the O 1s binding energy region were found to be 530.6 and 531.8 eV, respectively. A similar study has been reported in the literature.[35,36] The high-resolution XPS spectra that were employed to verify the valence state of the Cr species within the $CaCrO_4$ structure are shown in Figure 7c. The Cr 2p spectrum was deconvolved into four peaks, and the best fit was obtained. The Cr 2p spectrum contains two doublets, $2p_{3/2}$ and $2p_{1/2}$, Peaks at 576.4 and 586.5 eV were attributed to Cr (III) $2p_{3/2}$ and $2p_{1/2}$, respectively, while peaks at 579.9 and 588.9 eV were assigned to Cr (III) $2p_{3/2}$ and Cr (III) $2p_{1/2}$, respectively (VI). Most of the adsorbed Cr (VI) anions were reduced to Cr (III) through oxidation, followed by adsorption and complexion with oxygen-containing functional groups.[35] The wider Cr (VI) peaks confirm the formation of $CaCrO_4$. As shown in Figure 7d, the Ca 2p XPS spectrum of $CaCrO_4$ also splits up into two sublevels, $2p_{3/2}$ and $2p_{1/2}$, which are located at 347 and 351 eV, respectively.

**3.2. Photocatalytic Analysis.** *3.2.1. Optical Band Gap Study.* The optical properties and band structure of the synthesized $CaCrO_4$ photocatalyst were examined using UV analysis and depicted in Figure 8. The Tauc equation was used to figure out the band gap energy.[37]

$$(\alpha h\nu)^2 = A((h\nu - E_g)^n \quad (3)$$

In eq 3, n depends on the nature of the transition h$\nu$ is the energy of the incident photon Eg and $\alpha$ indicates the band gap energy and adsorption coefficient. Here, the band gap energy of $CaCrO_4$ has been estimated by plotting $(\alpha h\nu)^2$ against $E_g$. The value of band gap energy is found to be in the range of 1.928 eV, which was consistent with the first principle study as reported earlier.[38] Valence bands in $ABO_4$ structures may hybridize, leading to a reduced band gap. As a result, valence bands (VB) diffused, boosting the mobility of electron–hole pairs. Therefore, hybridization is considered advantageous for the redox reaction, which assists the photocatalytic process.[39]

*3.2.2. Photodegradation Mechanism.* Figure 9a–d depicts the UV–visible induced profile for the photodegradation of rhodamine B (RhB) with different contents of $CaCrO_4$ catalyst (5, 20, 35, and 50 mg), respectively. The UV–visible spectrum of RhB dye exhibits a strong adsorption band at 554 nm.

In the absence of the photocatalyst, the dye concentration did not change significantly, indicating that the photosensitization effect of RhB itself can be excluded. However, after the addition of photocatalyst to 15 mL of 5 ppm dye solution and the exposition to sunlight, the adsorption spectra


https://doi.org/10.1021/acsomega.3c02457
ACS Omega 2023, 8, 30095–30108

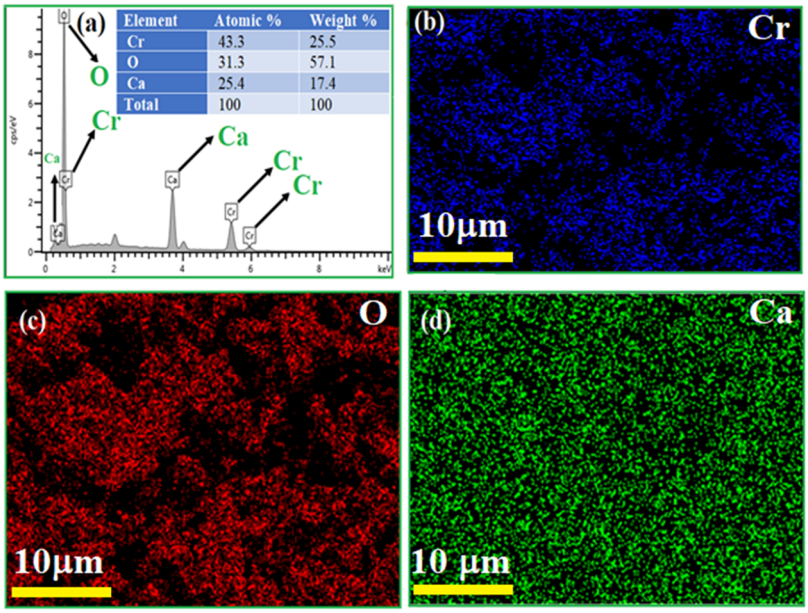


**Figure 6.** Energy-dispersive X-ray spectroscopy. (a) spectrum and (b–d) elemental mappings of the $CaCrO_4$ photocatalyst.

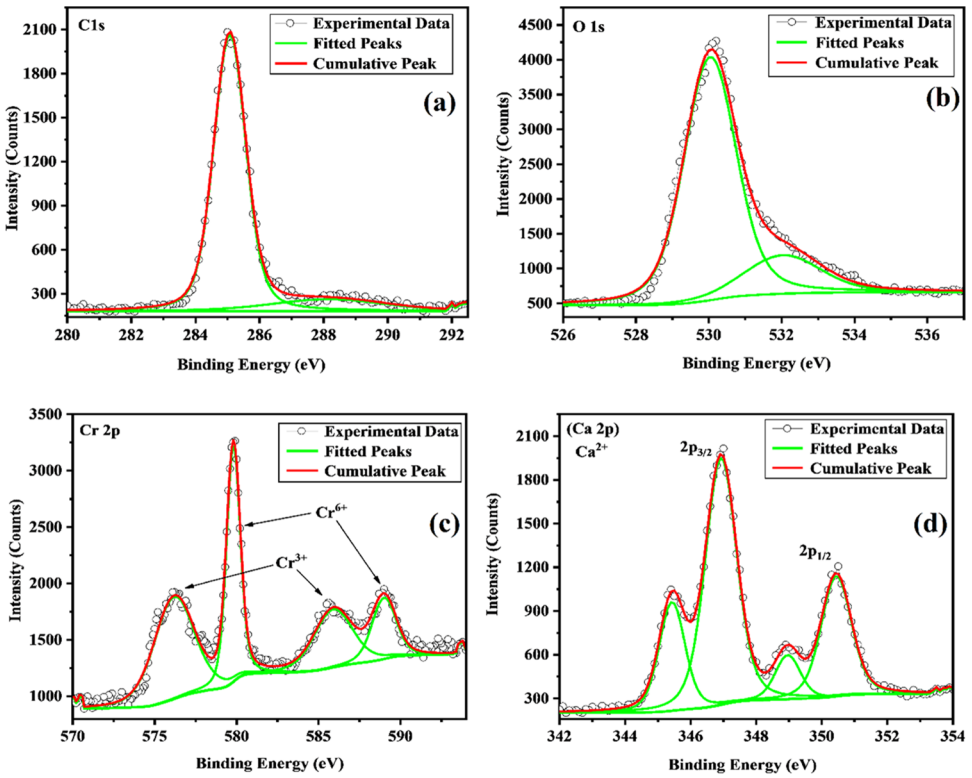


**Figure 7.** XPS spectra of $CaCrO_4$: (a) C 1s, (b) O 1s, (c) Cr 2p, and (d) Ca 2p elements.

exhibit a decreasing trend with irradiation time in all catalyst concentrations, indicating the photodegradation of RhB dye pollutants. From Figure 9, it was observed that the initial degradation rate was slow for 5 mg content of catalyst concentration and gradually increased with the increase in catalyst concentration from 20–35 mg, which may be due to the small rate of generation of electron–hole pairs at low catalyst concentrations, resulting in fewer radically active sites are available for the photodegradation process. However, with the increase of catalyst concentrations, the photogenerated electron–hole pairs increased, leading to an increase in the hydroxyl groups and the number of local active sites on the surface of the photocatalyst, which favored the photodegradation process.[40] The highest degradation rate was achieved with a 35 mg concentration of catalyst and the degradation profile was almost flat, demonstrating that the dye molecules have been destroyed under the action of the catalyst. However, further increasing the catalyst amount to 50 mg, caused the solution to become turbid and blocked UV radiation, leading to a decrease in the degradation process, as


https://doi.org/10.1021/acsomega.3c02457
ACS Omega 2023, 8, 30095–30108

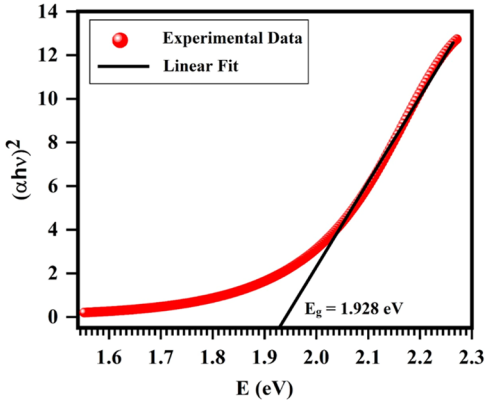


**Figure 8.** Tauc plot of CCO chromite nanoparticles.

shown in Figure 9d. As the degradation process involves photochemical reactions on the surface of the CaCrO4 catalyst, its specific surface area, size, and dispersion in the water solution may play a significant role in the degradation of organic pollutants.[41]

*3.2.3. Effect of Contact Time.* The irradiation time plays a significant role in the elimination of pollutants which affects the degradation efficiency of the $CaCrO_4$ photocatalyst. The degradation of RhB dye by using the photocatalyst and its efficacy has been measured by

$$\eta = \left(1 - \frac{A_t}{A_0}\right) \tag{4}$$

Here, $\eta$ labels the degradation efficiency, $A_0$ is the initial dye concentration, and $A_t$ is the dye concentration at a specific interval of time. The efficacy of different contents (5, 20, 35, and 50 mg) of $CaCrO_4$ on the photodegradation of dye was tested and shown in Figure 10a–d, respectively. It is generally observed that the photodegradation efficiency increases with irradiation time. The degradation efficiency ranges from 10 to 70.63, 10 to 80.73, and 20 to 93.55% for $x$ = 5, 20, and 35 mg, respectively, over the irradiation time ranging from 20 to 140 min. The most significant decolonization of RhB was observed with the catalyst concentration of 35 mg with an irradiation time of 140 min. This might be due to the passage of irradiation time photogenerated electron–hole pairs are enhanced and hence more hydroxyl groups with active sites are generated which assisted more adsorption of reactants on the surface of the photocatalyst which finally results in the degradation of organic dye pollutants. The degradation efficacy was decreased with increasing catalyst concentration and found to be in the range of 10–68.72% with an irradiation time of 20–140 min at $x$ = 50 mg as shown in Figure 10d. The decrease in degradation efficacy might be at a higher catalyst loading causing agglomeration and depletion in the penetration of light with a surplus amount of $CaCrO_4$ which may affect the photocatalytic performance.[42] Based on the literature, different photocatalysts have been reported for the degradation of different kinds of organic pollutants with variable irradiation times. A comparison has been made with the published results for their degradation rates to investigate the true effectiveness of the synthesized catalyst, and the outcomes are summarized in Table 2. From the tabulated values, it can be evident that the prepared catalyst demonstrates a significant degradation rate in comparison to the reported one with short irradiation times under visible light, which might be critical for industrial-scale applications.

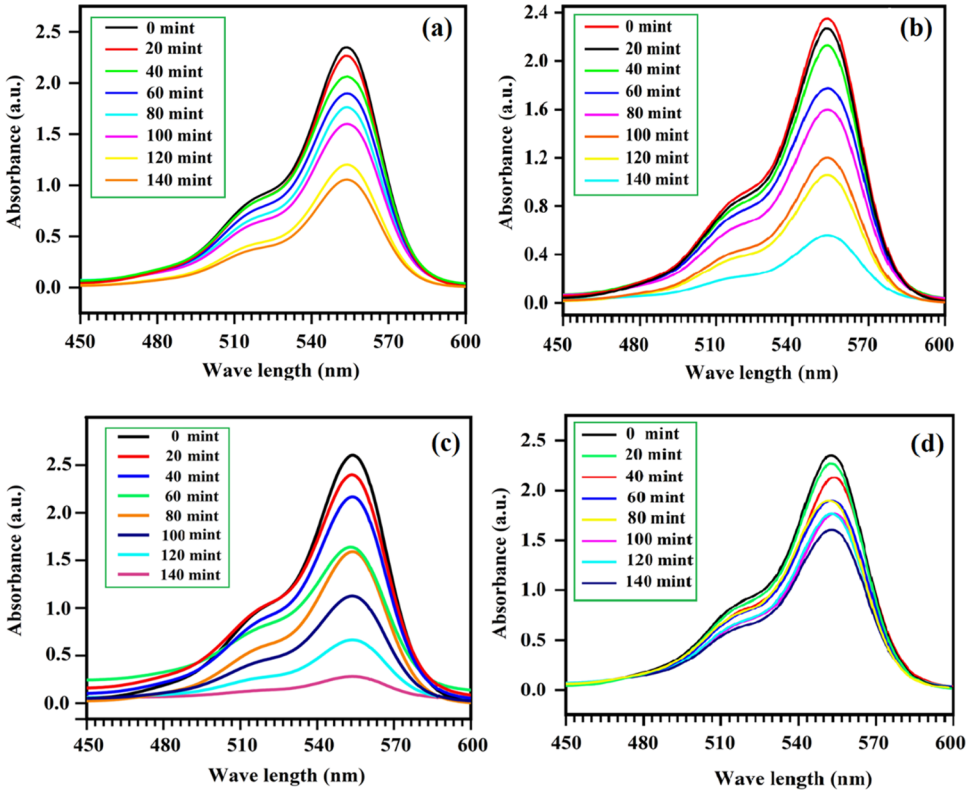


**Figure 9.** Time-dependent absorption spectra of RhB solution in visible light with different catalyst concentrations: (a) 5 mg, (b) 20 mg, (c) 35 mg, and (d) 50 mg.



https://doi.org/10.1021/acsomega.3c02457
ACS Omega 2023, 8, 30095–30108

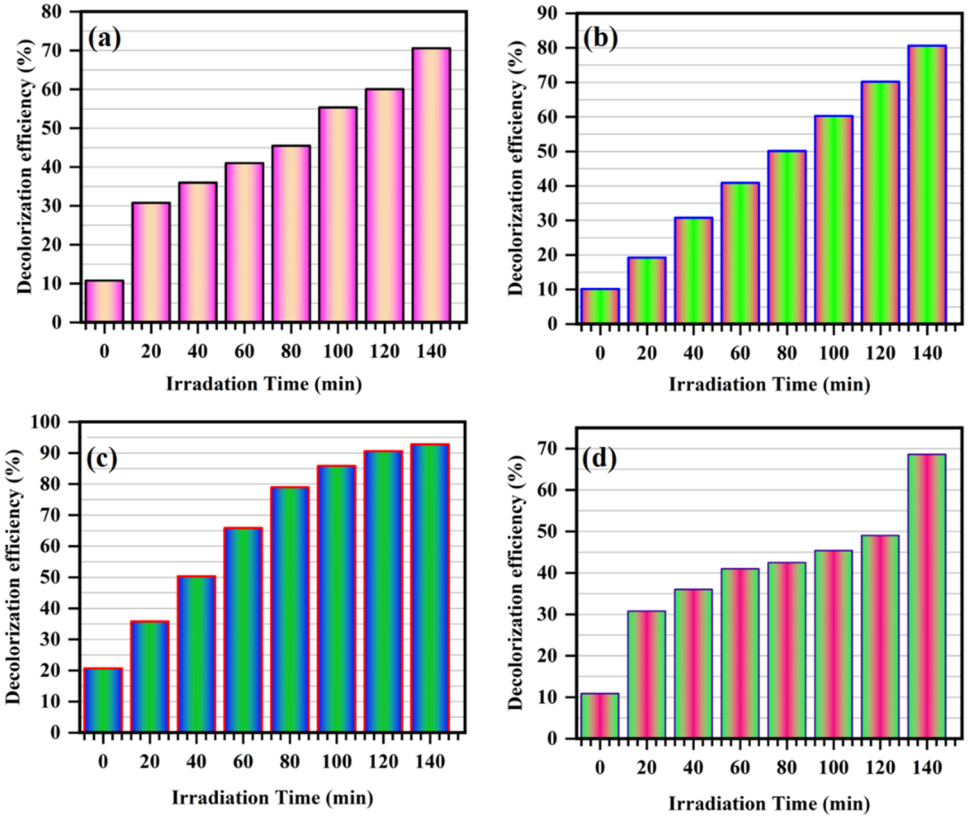


**Figure 10.** Degradation efficacy profile of RhB under solar light irradiation with different catalyst concentrations: (a) 5 mg, (b) 20 mg, (c) 35 mg, and (d) 50 mg.

**Table 2. Comparison of the Published and Synthesized Catalysts Degradation Rates as a Function of Exposure Time**

| photocatalyst | dye degraded | degradation % | degradation time (min) | light source | references |
|---|---|---|---|---|---|
| $BiVO_4$ | MB | 81 | 240 | visible | 43 |
| $SrWO_4/Bi_2O_3$ | MB | 99 | 180 | visible | 44 |
| BiVO4 | RhB | 22 | 240 | visible | 45 |
| $InBi_3$ $(MoO_6)_2$ | MB | 95 | 180 | visible | 39 |
| $Bi_2O_3$-$CeO_2$ | RhB | 73 | 200 | visible | 46 |
| Cu@$TiO_2$ | RhB, MB, MO | 95, 91, 89 | 180 | visible | 47 |
| $CaCrO_4$ | RhB, MB, MO | 93,86,72 | 140 | visible | present study |

*3.2.4. Effect of Catalyst Content.* The amount of catalyst plays a significant influence on the photodegradation rate. In the present study, the percentage decolorization efficiency of $CaCrO_4$ catalyst on the photodegradation of RhB with various concentrations from 5−50 mg as shown in Figure 10a−d, respectively. It can be visualized from the figure that with the increase in catalyst concentration from 5−15 mg, the rate of degradation was enhanced up to an optimum level of 93.55%. This might be due to the increase in the adsorption rate of photons and the number of dye molecules with the increase in catalyst concentration which resultantly increased the density of molecules in the area of illumination and hence photodegradation was enhanced. Moreover, the degradation efficiency of $CaCrO_4$ was observed to be decreased to 68.5240% for 50 mg catalyst content as shown in Figure 10d.

The decrease in degradation efficiency with the increase in catalyst concentration above the optimum level may occur due to the aggregation of catalyst particles which may decrease the active sites and increase the light-scattering effects of the catalyst particle.[48] Another reason may be the reduction of the passage of radiation through the catalyst and the available dye molecule is insufficient for adsorption compared to the number of catalyst molecules which causes degradation of reaction rates beyond a certain limit.[49] Thus, the optimum concentration of the $CaCrO_4$ catalyst in the present study was observed to be 35 mg.

*3.2.5. Comparison of the Degradation Rate of Different Organic Pollutants.* To investigate the true effectiveness of the photocatalyst the photocatalytic response of the $CaCrO_4$ towards the degradation of methylene blue (MB) and methyl orange (MO) dyes together with a colorless antibiotic pollutant has been examined. The photocatalytic degradation profiles of organic dye pollutants (RhB, MB, and MO) at optimum catalyst concentration (35 mg) under visible light irradiation are depicted in Figure 11a−c. The RhB and MB belong to the family of cations dye while MO is to anions dye. From Figure 11a,b, the adsorption peak for RhB and MB is at 554 and 570 nm, respectively, which decreases rapidly with irradiation time and almost becomes flattened at 140 min. However, the characteristic adsorption peak of MO which is situated at 464 nm only decreases slightly with the exposure time as shown in Figure 11c. The experimental degradation


https://doi.org/10.1021/acsomega.3c02457
ACS Omega 2023, 8, 30095−30108

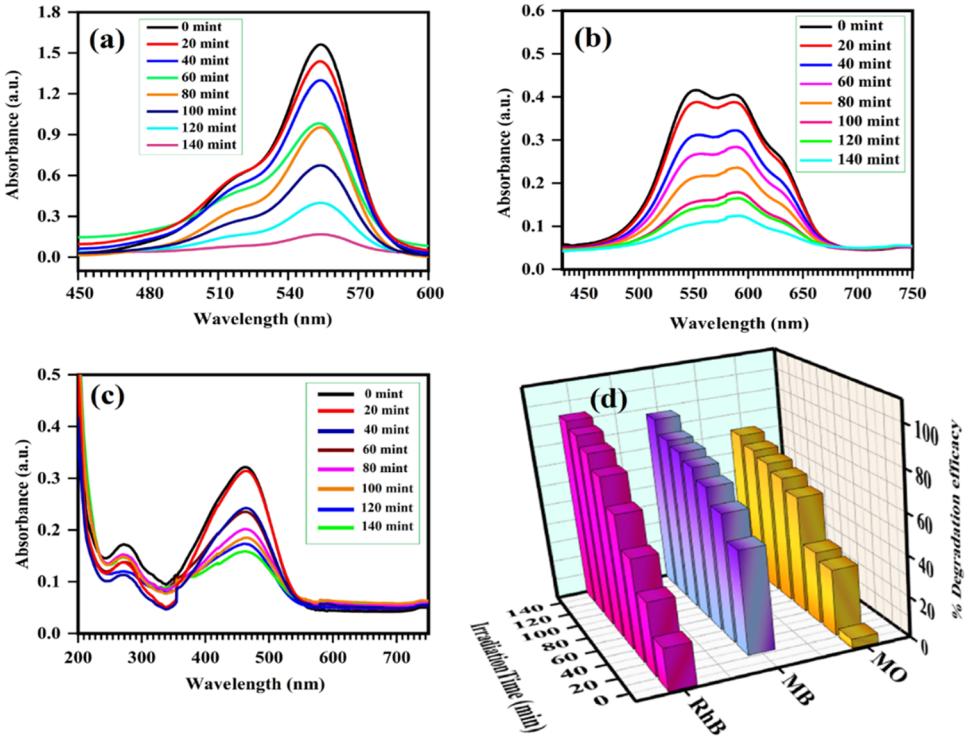


**Figure 11.** (a–c) Degradation profile of RhB, MB, and MO at optimum dosage of the catalyst (35 mg). (d) Comparison of degradation rates.

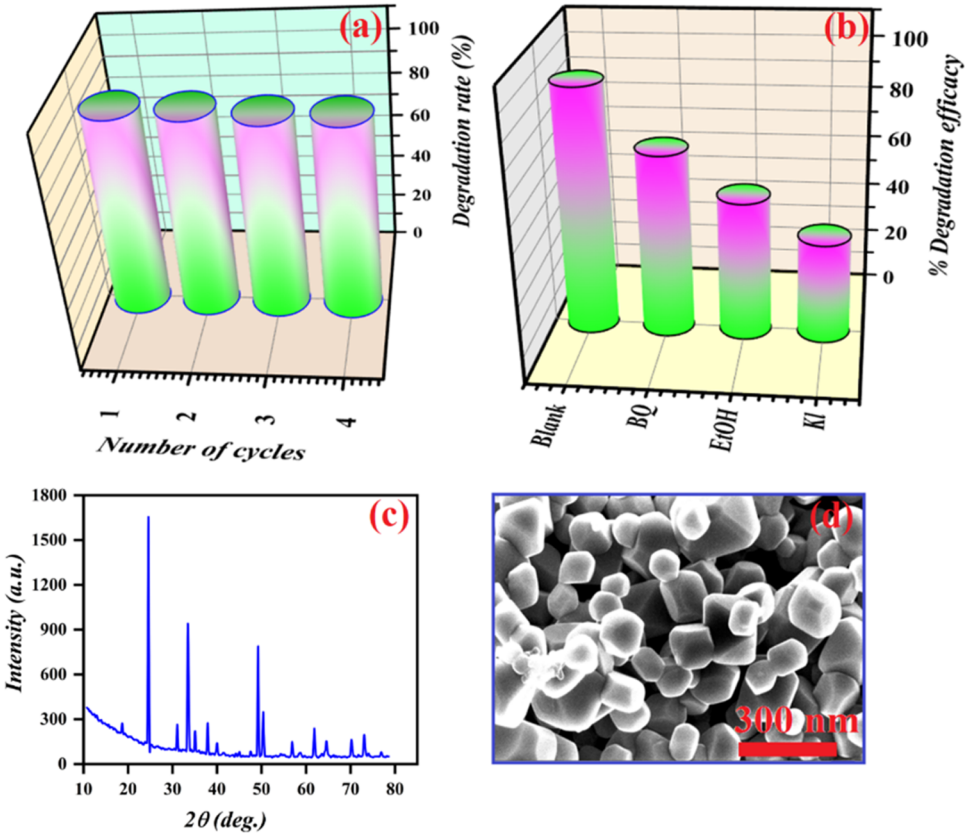


**Figure 12.** (a) cyclic test for RhB degradation by the $CaCrO_4$ (b) free radical scavenger test (c, d) phase and morphology of the used catalyst.

results deduced from the degradation data indicate that the $CaCrO_4$ photocatalyst exhibits significant degradation activity in the visible light region for cation dyes but shows a poor response for anion dye which might be attributed due to the charge on the surface of the photocatalyst, variation in the chemical structure and molecular weight of organic dyes. Additionally, it manipulates the reactivity between the organic dyes and OH, which may change the adsorption properties and



https://doi.org/10.1021/acsomega.3c02457
ACS Omega 2023, 8, 30095−30108

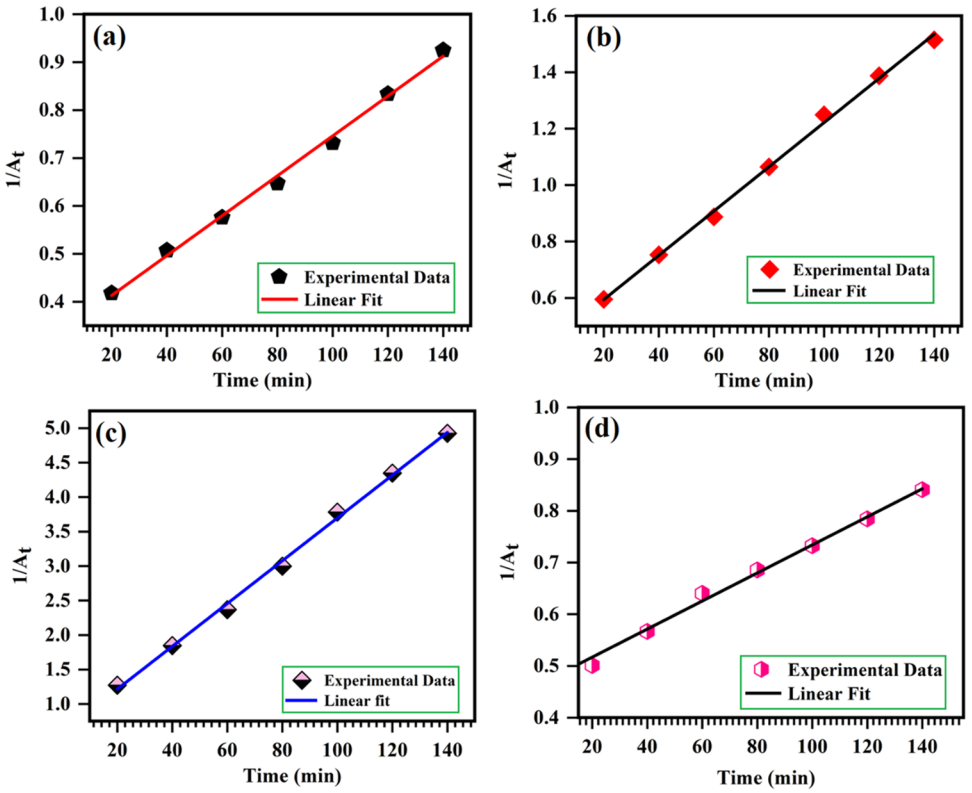


**Figure 13.** Kinetic analysis of RhB with different catalyst concentrations: (a) 5 mg, (b) 20 mg, (c) 35 mg, and (d) 50 mg.

ultimately limit the rate of photocatalytic reaction. The degradation rate was found to be 93.80 and 86.77% for RhB and MB, respectively, while MO degraded to 72.40% under the same condition as shown in Figure 11d. A possible pathway for the degradation of dyes has been proposed as follows

$$CaCrO_4 + h\nu \rightarrow e^- + h^+ \quad (5)$$

$$O_2 + e^- \rightarrow O_2^{\bullet -} \quad (6)$$

$$O_2^{\bullet -}H_2O \rightarrow HO_2^{\bullet} \quad (7)$$

$$H_2O/OH + h^+ \rightarrow {}^{\bullet}OH \quad (8)$$

$$O_2^{\bullet}/H_2O_2^{\bullet}/OH^{\bullet} + \text{RhB} \rightarrow CO_2 + H_2O + \text{byproduct of RhB} \quad (9)$$

*3.2.6. Reusability of the Photocatalyst.* To ensure the practical applicability of the photocatalyst, the RhB recycling experiment was conducted under visible light, and the outcome is depicted in Figure 12a. From the recycling analysis, it has been observed that the degradation rate was almost retained at the end of three cycles. After every cycle, the photocatalyst was centrifuged, washed, and dried before being reused for subsequent deterioration. The removal rate slightly decreased from 93.80 to 92.55% respectively. To investigate the true effectiveness of the recovered catalyst phase, morphological analysis was performed, and no variation was observed after three cycles as shown in Figure 12c,d which demonstrates the reusability and efficacy of the photocatalyst for practical applications.

*3.2.7. Detection of Active Species.* To investigate the role of primary active sites, degradation pathways, and principal active species responsible for the degradation of RhB dye molecules, a scavenger test has been carried out. From Figure 12b, it can be visualized that scavengers cause a decrease in degradation efficacy as the active species become deactivated. In the absence and presence of various scavengers such as BQ (benzoquinone, an $O_2^-$ quencher), EtOH (ethanol, a hydroxyl quencher), and KI (potassium iodide, OH, and hole radical quencher), degradation effectiveness was monitored under optimum conditions. The Figure shows that the deterioration level of RhB has decreased from 72.10, 54.60, and 39.31 after the addition of BQ, EtHO, and Kl separately. This type of behavior might be attributed to the suppression of reactive oxygen species within the sight of scavengers, which causes the formation of $O_2^{\bullet -}$ and •OH species that are effectively linked with the photodegradation of RhB.[44]

*3.2.8. Kinetic Analysis.* Kinetic studies play an influential role in determining the thermodynamic feasibility as well as rate-control parameters of the adsorption process.[50] In the present study, to investigate the synergetic adsorption-photodegradation process of RhB, three kinetic models were employed namely pseudo-first-order (PFO), pseudo-second-order (PSO), and intraparticle diffusion model (IPD). Generally, the validity of these models is based on the regression coefficient ($R^2$) value. From the kinetic evaluation of the observed degradation results of the $CaCrO_4$ catalyst, it has been found that the obtained $R^2$ values for the PSO model were higher than those for the PFO and IDP models. This suggests that the PSO model is well suited to fit photo-degradation experimental data. The linear form of the PSO model can be expressed as[51]

$$\frac{1}{A_t} = \frac{1}{A_0} + k_2 t \quad (10)$$



https://doi.org/10.1021/acsomega.3c02457
ACS Omega 2023, 8, 30095−30108

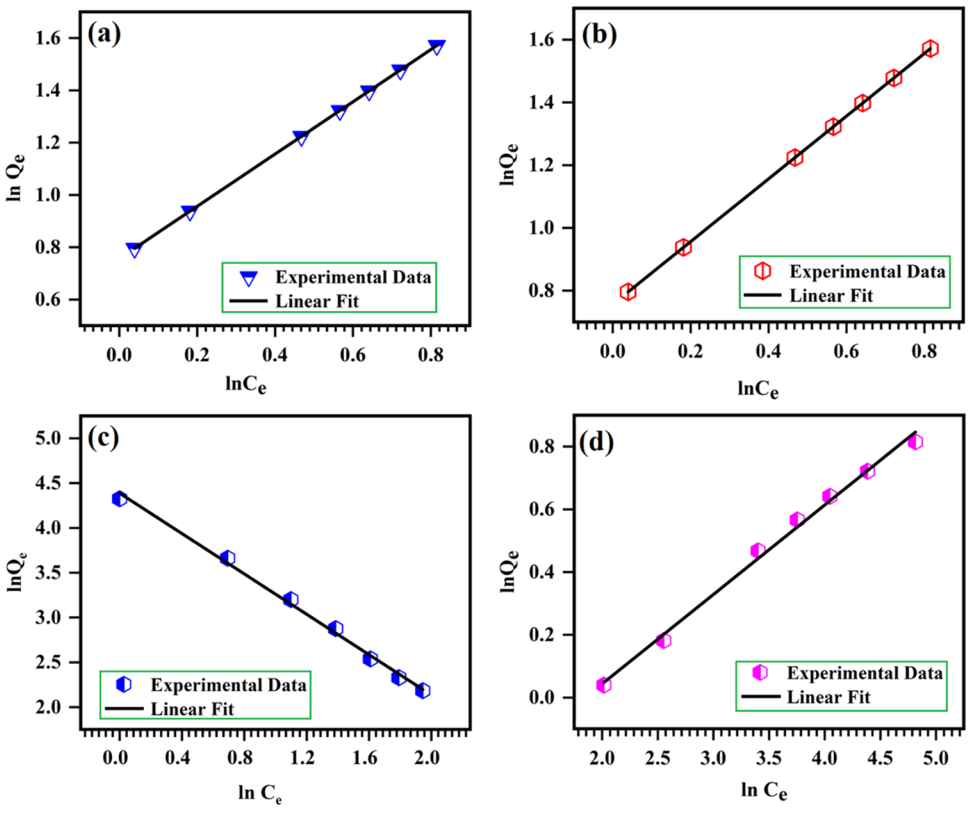


**Figure 14.** Isotherm analysis of RhB dye solution under different catalyst concentrations: (a) 5 mg, (b) 20 mg, (c) 35 mg, and (d) 50 mg.

In eq 10, $\frac{1}{A_0}$ refers to the initial concentration of dye at $t = 0$, $\frac{1}{A_t}$ indicates the dye concentration at $t = t$, $k_2$ is the second-order rate constant, and $t$ is the time. The PSO kinetic model for different concentrations of $CaCrO_4$ catalyst is shown in Figure 13a–d. In general, the value of the rate constant has been significantly influenced by the catalyst loading. From the PSO kinetic analysis of $CaCrO_4$, it has been evident that with the increase in catalyst concentration, the value of the rate constant increased. Initially, at a low catalyst concentration (5 mg), the value of the rate constant was small. But with the increase in catalyst concentration, the rate constant was enhanced, and a significant rate constant was achieved with 35 mg catalyst with a time irradiation of 140 min. In the PSO model, the adsorption and chemisorption are generally governed by the number of active sites on the surface of the adsorbent. With a small content of catalyst, few adsorption sites are available for dye molecules to adsorb at the surface of the catalyst, which may result in a reduction in the formation of hydroxyl radicals on the surface of the catalyst, leading to a lower degradation rate constant value. As the catalyst concentration increases from 5–35 mg, the value of the rate constant increases from 0.066–0.087 $min^{-1}$. This may occur due to the reason that with the increase in solute content, the recombination rate of electron–hole pairs is enhanced and the surface area may alter, which might increase the number of possible interactions between sorbent–sorbate and pore sites on the adsorbent surface and may assist the degradation rate. Beyond the optimum level (35 mg) the value of the rate constant was decreased (0.072 $min^{-1}$). This could be due to the high dose of catalyst, which results in the inactivation of activated molecules by interactions with ground-state molecules. The obtained kinetic parameters are within reliable ranges, which indicates a favorable nature of the adsorption process. Hence, the existing results are consistent with the PSO assumption. A similar trend was observed in the degradation data, indicating that the kinetic study is in close agreement with the degradation analysis.

*3.2.9. Adsorption Isotherm Analysis.* The investigation of isotherms is critical for comprehending the equilibrium relationship between organic dye pollutants and photocatalyst surfaces. In this study, the efficiency of adsorption isotherms has been investigated using the Langmuir, Freundlich, and Temkin models. According to the linear fitting results from three isotherm models, the regression coefficient value for Langmuir was higher than for the Temkin and Freundlich models, indicating that the Langmuir isotherm has significantly characterized adsorption behavior. The linear form of the Langmuir model can be expressed by[52]

$$\frac{C_e}{Q_e} = \frac{1}{Q_{mK_L}} + \frac{1}{Q_m}C_e \tag{11}$$

In eq 10, $C_e$ labels the catalyst equilibrium concentration, $Q_e$ refers to the amount of adsorbed dyes at equilibrium, $Q_m$ is the maximum monolayer adsorption capacity, and $K_L$ is the Langmuir isotherm constant. The Langmuir isotherm profile for different concentrations of catalyst (5–50 mg) is depicted in Figure 14a–d. From the isotherm investigation it has been observed that as the catalyst content was increased from 5–35 mg, the adsorption capacity was enhanced and was found to be in the range of 19.152–21.125 mg/g, respectively. This type of behavior in Langmuir isotherm data indicates that at low catalyst concentrations, few active sites and functional groups are accessible for adsorption, which results in a low adsorption capacity. As the catalyst loading increased the adsorption


https://doi.org/10.1021/acsomega.3c02457
ACS Omega 2023, 8, 30095–30108

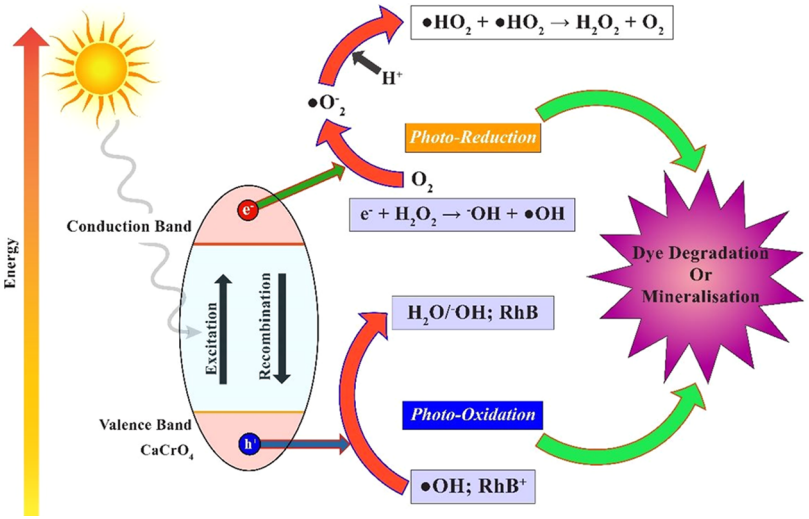


**Figure 15.** Proposed mechanism for photocatalytic degradation of RhB.

capacity enhanced, which might be the reason for the formation of a large number of binding sites and homogeneous adsorption taking place at the surface of the catalyst which may assist the photocatalytic process as a result adsorption capacity may improve. Beyond the optimum level of catalyst concentration (35 mg), the value of adsorption capacity was decreased to 20.124 mg/g for 50 mg of catalyst. This may occur due to the reason that at a higher concentration, the surface area of the catalyst may get saturated which causes the blockage of UV radiation which may be sensitive to the adsorption process. The dimensionless separation growth factor RL defines the adsorbate-adsorbent affinity and provides insights into the favorability of the adsorption process, which can be approximated by the relation[53]

$$R_L = \frac{1}{1 + K_L C_0} \tag{12}$$

Here, $C_0$ is the initial concentration of RhB dye and $K_L$ is the Langmuir equilibrium constant. In general, growth factor values between 0 and 1 signify that the adsorption process is favorable.[54] The observed value of $R_L$ is found to be 0.745, 0.823, 0.987, and 0.966 for 5, 20, 35, and 50 mg contents of the catalyst, respectively. It further exemplifies the favorable character of the adsorption process. The estimated isothermal parameters are in the liable range, which suggests that the isotherm analysis is consistent with the Langmuir assumption. Hence, the isotherm study is consistent with the kinetic analysis.

*3.2.10. Possible Photocatalytic Mechanism.* Based on the experimental results, conceivable dye degradation mechanics have been hypothesized and schematically elucidated in Figure 15, which shows the photocatalytic degradation of RhB using $CaCrO_4$ photocatalyst. The first step in the photocatalytic process is the generation of exciton pairs after the irradiation of the sample with visible light irradiation and the formation of hydroxyl radicals (•OH) and superoxide radical anions ($O_2^-$). Due to their strong oxidative capabilities, these radicals oxidized RhB. The (•OH) radical is regarded to be the most effective oxidizing agent in the photodegradation process. Electron−hole pairs react with the by-products $CO_2$ and $H_2O$ to form highly reactive hydroxyl and superoxide radicals. The adsorbed oxygen ($O_2^{\bullet-}$) on the catalyst surface is trapped with an electron which further reacts with $H_2O$ to generate $H_2O^{\bullet}$ radicals. Finally, the generated hydroxyl radicals on the surface of the photocatalyst decompose the RhB dye into $H_2O$ and $CO_2$ and their by-products. A radical trapping experiment reinforces the mechanism. The combination of superoxide and hydroxyl radicals may effectively mineralize RhB. A similar mechanism has been postulated for MB and MO.

## 4. CONCLUSIONS

The current study successfully employed the sol−gel auto-combustion method to synthesize the $CaCrO_4$ chromite. The characterization analysis including XRD, FT-IR, FESEM, EDX, UV, and XPS confirmed the single-phase formation, crystal structure, chemical composition, band gap energy, and oxidation state of the catalyst. The $CaCrO_4$ catalyst showed efficient photodegradation of RhB dye ranging from 10−70.63, 10−80.73, 20−93.55, and 10−68.72% for different catalyst concentrations of 5, 20, 35, and 50 mg with the irradiation time of 20−140 min, respectively. A comparison between cationic and anionic dyes demonstrates that the photocatalytic response is higher for the cation dye (RhB 93.80%, MB 86.77%) than for the anionic dye (MO 72.40%). The adsorption isotherm analysis revealed that the Langmuir model fitted well with the experimental data, with an adsorption capacity ranging from 19.152 to 21.125 mg/g for the catalyst concentration of 5−35 mg. The kinetic analysis indicated that the pseudo-second-order model was the most appropriate approach for explaining the adsorption process, with a rate constant ranging from 0.066 to 0.087 $min^{-1}$. Based on the present findings, $CaCrO_4$ has demonstrated its potential application as an effective photocatalyst for the degradation of rhodamine B dye from wastewater. The recycling result indicates significant reusability up to three cycles, demonstrating their use in particle applications. The scavenging test indicates that $\bullet O_2^-$ and •OH are the governing species in the mineralization of RhB. Further studies can be conducted to explore the feasibility of $CaCrO_4$ for the degradation of other organic pollutants and to optimize the operational parameters for practical applications.


https://doi.org/10.1021/acsomega.3c02457
ACS Omega 2023, 8, 30095−30108

## AUTHOR INFORMATION


### Corresponding Authors

**Muhammad Javed** − *Department of Physics, University of Kotli Azad Jammu and Kashmir, Kotli 11100, Pakistan*; Email: Javedbinyousuf@gmail.com

**Ayaz Arif Khan** − *Department of Physics, University of Azad Jammu and Kashmir, Muzaffarabad 13100, Pakistan*; Email: ayazbinarif@gmail.com

**Muhammad Aniq Shazni Mohammad Haniff** − *Institute of Microengineering and Nanoelectronics, Universiti Kebangsaan Malaysia, 43600 Bangi, Selangor, Malaysia*; orcid.org/0000-0003-3980-3460; Email: aniqshazni@ukm.edu.my

### Authors

**Naeem Akbar** − *Department of Physics, University of Kotli Azad Jammu and Kashmir, Kotli 11100, Pakistan*

**Asad Masood** − *Institute of Microengineering and Nanoelectronics, Universiti Kebangsaan Malaysia, 43600 Bangi, Selangor, Malaysia*

**Naeem Ahmed** − *Institute of Microengineering and Nanoelectronics, Universiti Kebangsaan Malaysia, 43600 Bangi, Selangor, Malaysia*

**Raja Yasir Mehmood** − *National Institute of Lasers and Optronics College, Pakistan Institute of Engineering and Applied Sciences, Islamabad 45650, Pakistan*

**Said Nasir Khisro** − *Department of Physics, University of Kotli Azad Jammu and Kashmir, Kotli 11100, Pakistan*

**Muhammed Ali Shaikh Abdul** − *Fuel Cell Institute, Universiti Kebangsaan Malaysia, 43600 Bangi, Selangor, Malaysia*

**Attaullah Shah** − *National Institute of Lasers and Optronics College, Pakistan Institute of Engineering and Applied Sciences, Islamabad 45650, Pakistan*

Complete contact information is available at: https://pubs.acs.org/10.1021/acsomega.3c02457


### Notes

The authors declare no competing financial interest.

## ACKNOWLEDGMENTS

The authors acknowledge the funding support provided by Universiti Kebangsaan Malaysia (UKM) through a Geran Universiti Penyelidikan (GUP) with code GUP-2021-070, a Geran Galakan Penyelidik Muda (GGPM) with code GGPM-2020-044 and GGPM-2021-058/1. The authors would also like to express their gratitude to the Centre for Research and Instrumentation Management at Universiti Kebangsaan Malaysia for providing excellent facilities.

## REFERENCES


(1) Rathi, B. S.; Kumar, P. S.; Vo, D.-V. N. Critical Review on Hazardous Pollutants in Water Environment: Occurrence, Monitoring, Fate, Removal Technologies and Risk Assessment. *Sci. Total Environ.* **2021**, *797*, No. 149134.

(2) Tkaczyk, A.; Mitrowska, K.; Posyniak, A. Synthetic Organic Dyes as Contaminants of the Aquatic Environment and Their Implications for Ecosystems: A Review. *Sci. Total Environ.* **2020**, *717*, No. 137222.

(3) Kumar, S.; Karthikeyan, S.; Lee, A. F. G-C3N4-Based Nanomaterials for Visible Light-Driven Photocatalysis. *Catalysts* **2018**, *8*, No. 74.

(4) Boettcher, S. W.; Mallouk, T. E.; Osterloh, F. E. Themed Issue on Water Splitting and Photocatalysis. *J. Mater. Chem. A* **2016**, *4*, 2764−2765.

(5) Fardood, S. T.; Moradnia, F.; Forootan, R.; Abbassi, R.; Jalalifar, S.; Ramazani, A.; Sillanpää, M. Facile Green Synthesis, Characterization and Visible Light Photocatalytic Activity of MgFe2O4@CoCr2O4 Magnetic Nanocomposite. *J. Photochem. Photobiol. A: Chem.* **2022**, *423*, No. 113621.

(6) Mandal, S. K.; Dutta, K.; Pal, S.; Mandal, S.; Naskar, A.; Pal, P. K.; Bhattacharya, T.; Singha, A.; Saikh, R.; De, S. Engineering of ZnO/RGO Nanocomposite Photocatalyst towards Rapid Degradation of Toxic Dyes. *Mater. Chem. Phys.* **2019**, *223*, 456−465.

(7) Moradnia, F.; Fardood, S. T.; Ramazani, A.; Min, B.; Joo, S. W.; Varma, R. S. Magnetic Mg0. 5Zn0. 5FeMnO4 Nanoparticles: Green Sol-Gel Synthesis, Characterization, and Photocatalytic Applications. *J. Cleaner Prod.* **2021**, *288*, No. 125632.

(8) Oller, I.; Malato, S.; Sánchez-Pérez, Ja. Combination of Advanced Oxidation Processes and Biological Treatments for Wastewater Decontamination—a Review. *Sci. Total Environ.* **2011**, *409*, 4141−4166.

(9) Abbas, A. A.; Jingsong, G.; Ping, L. Z.; Ya, P. Y.; Al-Rekabi, W. S. Review on LandWll Leachate Treatments. *J. Appl. Sci. Res.* **2009**, *5*, 534−545.

(10) Hanjra, M. A.; Blackwell, J.; Carr, G.; Zhang, F.; Jackson, T. M. Wastewater Irrigation and Environmental Health: Implications for Water Governance and Public Policy. *Int. J. Hyg. Environ. Health* **2012**, *215*, 255−269.

(11) Chan, S. H. S.; Yeong Wu, T.; Juan, J. C.; Teh, C. Y. Recent Developments of Metal Oxide Semiconductors as Photocatalysts in Advanced Oxidation Processes (AOPs) for Treatment of Dye Wastewater. *J. Chem. Technol. Biotechnol.* **2011**, *86*, 1130−1158.

(12) Lorenz, M.; Rao, M. R.; Venkatesan, T.; Fortunato, E.; Barquinha, P.; Branquinho, R.; Salgueiro, D.; Martins, R.; Carlos, E.; Liu, A. The 2016 Oxide Electronic Materials and Oxide Interfaces Roadmap. *J. Phys. D: Appl. Phys.* **2016**, *49*, No. 433001.

(13) Taghavi Fardood, S.; Moradnia, F.; Heidarzadeh, S.; Naghipour, A. Green Synthesis, Characterization, Photocatalytic and Antibacterial Activities of Copper Oxide Nanoparticles of Copper Oxide Nanoparticles. *Nanochem. Res.* **2023**, *8*, 134−140.

(14) Zhu, Y.; Zheng, G.; Dai, Z.; Zhang, L.; Ma, Y. Photocatalytic and Luminescent Properties of SrMoO4 Phosphors Prepared via Hydrothermal Method with Different Stirring Speeds. *J. Mater. Sci. Technol.* **2017**, *33*, 23−29.

(15) Ghoreishi, S. M. Facile Synthesis and Characterization of CaWO 4 Nanoparticles Using a New Schiff Base as Capping Agent: Enhanced Photocatalytic Degradation of Methyl Orange. *J. Mater. Sci.: Mater. Electron.* **2017**, *28*, 14833−14838.

(16) Long, Y.; Zhang, W.; Yang, L.; Yong, Y.; Yu, R.; Ding, S.; Liu, Y.; Jin, C. High-Pressure Induced Structural Phase Transition in CaCrO4: Evidence from Raman Scattering Studies, arXiv preprint cond-mat/0506129. 2005.

(17) El-Sheikh, S.; Rabah, M. Optical Properties of Calcium Chromate 1D-Nanorods Synthesized at Low Temperature from Secondary Resources. *Opt. Mater.* **2014**, *37*, 235−240.

(18) Nunes, D.; Pimentel, A.; Branquinho, R.; Fortunato, E.; Martins, R. Metal Oxide-Based Photocatalytic Paper: A Green Alternative for Environmental Remediation. *Catalysts* **2021**, *11*, No. 504.

(19) Kamble, G. S.; Ling, Y.-C. Solvothermal Synthesis of Facet-Dependent BiVO4 Photocatalyst with Enhanced Visible-Light-Driven Photocatalytic Degradation of Organic Pollutant: Assessment of Toxicity by Zebrafish Embryo. *Sci. Rep.* **2020**, *10*, No. 12993.

(20) Abbasi, A.; Keihan, A. H.; Golsefidi, M. A.; Rahimi-Nasrabadi, M.; Khojasteh, H. Synthesis, Characterization and Photocatalytic Activity of FeCr2O4 and FeCr2O4/Ag Nanocomposites. *J. Nanostruct.* **2020**, *10*, 518−530.

(21) Bakar, S. A.; Ribeiro, C. Nitrogen-Doped Titanium Dioxide: An Overview of Material Design and Dimensionality Effect over Modern Applications. *J. Photochem. Photobiol. C: Photochem. Rev.* **2016**, *27*, 1−29.

(22) Ghosh, S.; Sharma, A. D.; Basu, R. N.; Maiti, H. S. Influence of B Site Substituents on Lanthanum Calcium Chromite Nanocrystalline




https://doi.org/10.1021/acsomega.3c02457
*ACS Omega* 2023, 8, 30095−30108

Materials for a Solid-Oxide Fuel Cell. *J. Am. Ceram. Soc.* **2007**, *90*, 3741−3747.
(23) Sutka, A.; Mezinskis, G. Sol-Gel Auto-Combustion Synthesis of Spinel-Type Ferrite Nanomaterials. *Front. Mater. Sci.* **2012**, *6*, 128−141.
(24) Moradnia, F.; Fardood, S. T.; Ramazani, A.; Gupta, V. K. Green Synthesis of Recyclable MgFeCrO4 Spinel Nanoparticles for Rapid Photodegradation of Direct Black 122 Dye. *J. Photochem. Photobiol. A: Chem.* **2020**, *392*, No. 112433.
(25) Cheng, J.; Liu, C.; Cao, W.; Qi, M.; Shao, G. Synthesis and Electrical Properties of Scheelite Ca1− XSmxMoO4+ $\delta$ Solid Electrolyte Ceramics. *Mater. Res. Bull.* **2011**, *46*, 185−189.
(26) Dixit, P.; Chauhan, V.; Rai, S.; Pandey, P. C. Realization of Neutral White Light Emission in CaMoO4: 4Dy3+ Phosphor via Sm3+ Co-Doping. *J. Alloys Compd.* **2022**, *897*, No. 162820.
(27) Mustapha, S.; Ndamitso, M.; Abdulkareem, A.; Tijani, J.; Shuaib, D.; Mohammed, A.; Sumaila, A. Comparative Study of Crystallite Size Using Williamson-Hall and Debye-Scherrer Plots for ZnO Nanoparticles. *Adv. Nat. Sci.: Nanosci. Nanotechnol.* **2019**, *10*, No. 045013.
(28) Thandavan, T. M. K.; Gani, S. M. A.; Wong, C. S.; Nor, R. M. Evaluation of Williamson−Hall Strain and Stress Distribution in ZnO Nanowires Prepared Using Aliphatic Alcohol. *J. Nondestr. Eval.* **2015**, *34*, 1−9.
(29) Suzudo, T.; Tsuru, T. Inclination of Self-Interstitial Dumbbells in Molybdenum and Tungsten: A First-Principles Study. *AIP Adv.* **2021**, *11*, No. 065012.
(30) Gupta, G.; Rath, S. Microstructural Investigations of Green-Synthesized Wurtzite-Phase ZnMgO Nanopowders and Their Defect-Mediated Ferromagnetism. *Mater. Res. Bull.* **2022**, *148*, No. 111671.
(31) Chankhanittha, T.; Komchoo, N.; Senasu, T.; Piriyanon, J.; Youngme, S.; Hemavibool, K.; Nanan, S. Silver Decorated ZnO Photocatalyst for Effective Removal of Reactive Red Azo Dye and Ofloxacin Antibiotic under Solar Light Irradiation. *Colloids Surf., A* **2021**, *626*, No. 127034.
(32) Androš, L.; Jurić, M.; Popović, J.; Pajić, D.; Zadro, K.; Molčanov, K.; Žilić, D.; Planinić, P. 1D Heterometallic Oxalate Compounds as Precursors for Mixed Ca−Cr Oxides−Synthesis, Structures, and Magnetic Studies. *Eur. J. Inorg. Chem.* **2014**, *2014*, 5703−5713.
(33) Ivanova, T.; Gesheva, K.; Cziraki, A.; Szekeres, A.; Vlaikova, E. *Structural Transformations and Their Relation to the Optoelectronic Properties of Chromium Oxide Thin Films*; IOP Publishing, 2008; Vol. *113*, p 012030.
(34) Liu, N.; Wu, J.; Fei, F.; Lei, J.; Shi, W.; Quan, G.; Zeng, S.; Zhang, X.; Tang, L. Ibuprofen Degradation by a Synergism of Facet-Controlled MIL-88B (Fe) and Persulfate under Simulated Visible Light. *J. Colloid Interface Sci.* **2022**, *612*, 1−12.
(35) Ahmed, N.; Masood, A.; Siow, K. S.; Wee, M. M. R.; Haron, F. F.; Patra, A.; Nayan, N.; Soon, C. F. Effects of Oxygen (O 2) Plasma Treatment in Promoting the Germination and Growth of Chili. *Plasma Chem. Plasma Process.* **2022**, 1−18.
(36) Masood, A.; Ahmed, N.; Wee, M. M. R.; Patra, A.; Mahmoudi, E.; Siow, K. S. Atmospheric Pressure Plasma Polymerisation of D-Limonene and Its Antimicrobial Activity. *Polymers* **2023**, *15*, No. 307.
(37) Fardood, S. T.; Forootan, R.; Moradnia, F.; Afshari, Z.; Ramazani, A. Green Synthesis, Characterization, and Photocatalytic Activity of Cobalt Chromite Spinel Nanoparticles. *Mater. Res. Express* **2020**, *7*, No. 015086.
(38) Li, L.; Yu, W.; Long, Y.; Jin, C. First-Principles Calculations on the Pressure Induced Zircon-Type to Scheelite-Type Phase Transition of CaCrO4. *Solid State Commun.* **2006**, *137*, 358−361.
(39) Nie, X.; Wulayin, W.; Song, T.; Li, T.; Qiao, X. A Scheelite-Type Semiconductor InBi3 (MoO6) 2 Nanoparticles: Preparation, Structural and Optical Properties. *J. Taiwan Inst. Chem. Eng.* **2017**, *74*, 263−271.
(40) Jian, S.; Tian, Z.; Hu, J.; Zhang, K.; Zhang, L.; Duan, G.; Yang, W.; Jiang, S. Enhanced Visible Light Photocatalytic Efficiency of La-Doped ZnO Nanofibers via Electrospinning-Calcination Technology. *Adv. Powder Mater.* **2022**, *1*, No. 100004.
(41) Mahmood, H.; Khan, M.; Mohuddin, B.; Iqbal, T. Solution-Phase Growth of Tin Oxide (SnO2) Nanostructures: Structural, Optical and Photocatalytic Properties. *Mater. Sci. Eng.: B* **2020**, *258*, No. 114568.
(42) Rafaie, H. A.; Yusop, N. F. M.; Azmi, N. F.; Abdullah, N. S.; Ramli, N. I. T. Photocatalytic Degradation of Methylene Blue Dye Solution Using Different Amount of ZnO as a Photocatalyst. *Sci. Lett.* **2021**, *15*, No. 1.
(43) Kumar, M.; Vaish, R.; ben Ahmed, S. Piezo-photocatalytic Activity of Mechanochemically Synthesized BiVO4 for Dye Cleaning. *J. Am. Ceram. Soc.* **2022**, *105*, 2309−2322.
(44) Subalakshmi, A.; Kavitha, B.; Srinivasan, N.; Rajarajan, M.; Suganthi, A. An Affordable Efficient SrWO4 Decorated Bi2O3 Nanocomposite: Photocatalytic Activity for the Degradation of Methylene Blue under Visible Light Irradiation. *Mater. Today: Proc.* **2022**, *48*, 409−419.
(45) Zhang, Z.; Wang, W.; Shang, M.; Yin, W. Photocatalytic Degradation of Rhodamine B and Phenol by Solution Combustion Synthesized BiVO4 Photocatalyst. *Catal. Commun.* **2010**, *11*, 982−986.
(46) Wang, Q.; Yu, S.; Tan, Z.; Zhang, R.; Li, Z.; Gao, X.; Shen, B.; Su, H. Synthesis of Monodisperse Bi 2 O 3-Modified CeO 2 Nanospheres with Excellent Photocatalytic Activity under Visible Light. *CrystEngComm* **2015**, *17*, 671−677.
(47) Ethiraj, A. S.; Rhen, D. S.; Soldatov, A. V.; Ali, G. A.; Bakr, Z. H. Efficient and Recyclable Cu Incorporated TiO2 Nanoparticle Catalyst for Organic Dye Photodegradation. *Int. J. Thin Film Sci. Technol.* **2021**, *10*, 169−182.
(48) Iqbal, M.; Bhatti, H. N.; Younis, S.; Rehmat, S.; Alwadai, N.; Almuqrin, A. H.; Iqbal, M. Graphene Oxide Nanocomposite with CuSe and Photocatalytic Removal of Methyl Green Dye under Visible Light Irradiation. *Diamond Relat. Mater.* **2021**, *113*, No. 108254.
(49) Friedmann, D.; Mendive, C.; Bahnemann, D. TiO2 for Water Treatment: Parameters Affecting the Kinetics and Mechanisms of Photocatalysis. *Appl. Catal., B* **2010**, *99*, 398−406.
(50) Anju, S.; Yesodharan, S.; Yesodharan, E. Zinc Oxide Mediated Sonophotocatalytic Degradation of Phenol in Water. *Chem. Eng. J.* **2012**, *189*, 84−93.
(51) An, J.; Wang, X.; Li, Y.; Kang, W.; Lian, K. Polystyrene Nanofibers as an Effective Sorbent for the Adsorption of Clonazepam: Kinetic and Thermodynamic Studies. *RSC Adv.* **2022**, *12*, 3394−3401.
(52) Bameri, I.; Saffari, J.; Baniyaghoob, S.; Ekrami-Kakhki, M.-S. Synthesis of Magnetic Nano-NiFe2O4 with the Assistance of Ultrasound and Its Application for Photocatalytic Degradation of Titan Yellow: Kinetic and Isotherm Studies. *Colloid Interface Sci. Commun.* **2022**, *48*, No. 100610.
(53) Khairy, M. Synthesis, Characterization, Magnetic and Electrical Properties of Polyaniline/NiFe2O4 Nanocomposite. *Synth. Met.* **2014**, *189*, 34−41.
(54) Kannan, N.; Sundaram, M. M. Kinetics and Mechanism of Removal of Methylene Blue by Adsorption on Various Carbons—a Comparative Study. *Dyes Pigm.* **2001**, *51*, 25−40.


https://doi.org/10.1021/acsomega.3c02457
*ACS Omega* 2023, 8, 30095−30108